Originally published as:

RESEARCH ARTICLE

Special Section:
Particle Dynamics in the Earth's Radiation Belts

Key Points:
- Global computations of the (L, E, α_0) structure of the evolving radiation belt during quiet times agree well with observations
- The inner belt decay is pitch angle dependent, while the outer belt is much more homogeneous with two distinct (L, E) regions
- The homogeneity of the pitch angle diffusion coefficient due to hiss waves explains the uniform outer belt decay and why 1D and 3D simulations agree

Correspondence to:
J.-F. Ripoll,
jean-francois.ripoll@cea.fr

Observations and Fokker-Planck Simulations of the *L*-Shell, Energy, and Pitch Angle Structure of Earth's Electron Radiation Belts During Quiet Times

J.-F. Ripoll[1] (iD), V. Loridan[1] (iD), M. H. Denton[2,3] (iD), G. Cunningham[4,5] (iD), G. Reeves[4,5] (iD), O. Santolík[6,7,8,9] (iD), J. Fennell[10] (iD), D. L. Turner[10] (iD), A. Y. Drozdov[11] (iD), J. S. Cervantes Villa[12], Y. Y. Shprits[13,14,15] (iD), S. A. Thaller[16] (iD), W. S. Kurth[17] (iD), C. A. Kletzing[17] (iD), M. G. Henderson[18] (iD), and A. Y. Ukhorskiy[19] (iD)

[1]CEA, DAM, DIF, Arpajon, France, [2]New Mexico Consortium, Los Alamos, NM, USA, [3]Space Science Institute, Boulder, CO, USA, [4]Los Alamos National Laboratory, Los Alamos, NM, USA, [5]New Mexico Consortium, Los Alamos, NM, USA, [6]Department of Space Physics, Institute of Atmospheric Physics, The Czech Academy of Sciences, Prague, Czechia, [7]Faculty of Mathematics and Physics, Charles University, Prague, Czechia, [8]Institute of Atmospheric Physics ASCR, Prague, Czech Republic, [9]Faculty of Mathematics and Physics, Charles University, Prague, Czech Republic, [10]Space Sciences Department, The Aerospace Corporation, El Segundo, CA, USA, [11]Department of Earth, Planetary, and Space Sciences, University of California, Los Angeles, CA, USA, [12]Helmholtz Centre Potsdam, GFZ German Research Centre for Geosciences, Potsdam, Germany, [13]Helmholtz Centre Potsdam, GFZ German Research Centre for Geosciences, Potsdam, Germany, [14]Institute for Physics and Astronomy, University of Potsdam, Potsdam, Germany, [15]Department of Earth, Planetary, and Space Sciences, University of California, Los Angeles, CA, USA, [16]School of Physics and Astronomy, University of Minnesota, Minneapolis, MN, USA, [17]Department of Physics and Astronomy, University of Iowa, Iowa City, IA, USA, [18]Los Alamos National Laboratory, Los Alamos, NM, USA, [19]Applied Physics Laboratory, The Johns Hopkins University, Laurel, MD, USA

Abstract The evolution of the radiation belts in L-shell (L), energy (E), and equatorial pitch angle (α_0) is analyzed during the calm 11-day interval (4–15 March) following the 1 March 2013 storm. Magnetic Electron and Ion Spectrometer (MagEIS) observations from Van Allen Probes are interpreted alongside 1D and 3D Fokker-Planck simulations combined with consistent event-driven scattering modeling from whistler mode hiss waves. Three (L, E, α_0) regions persist through 11 days of hiss wave scattering; the pitch angle-dependent inner belt core ($L \sim {<}2.2$ and $E < 700$ keV), pitch angle homogeneous outer belt low-energy core ($L > {\sim}5$ and $E{\sim} < 100$ keV), and a distinct pocket of electrons ($L \sim [4.5, 5.5]$ and $E \sim [0.7, 2]$ MeV). The pitch angle homogeneous outer belt is explained by the diffusion coefficients that are roughly constant for $\alpha_0 \sim {<}60°$, $E > 100$ keV, $3.5 < L < L_{pp} \sim 6$. Thus, observed unidirectional flux decays can be used to estimate local pitch angle diffusion rates in that region. Top-hat distributions are computed and observed at $L \sim 3$–3.5 and $E = 100$–300 keV.

Plain Language Summary We study the evolution of the radiation belts during quiet geomagnetic times from satellite observations and numerical codes. We reach a global understanding of the trapped electrons variation with time, space, energy, and pitch angle (the angle of the velocity vector with the magnetic field). We exhibit three stable regions, which are less sensitive to scattering from hiss waves, while, on the other hand, hiss causes flux decay over 12 days that forms the slot region between the inner and outer belt. The existing theory explains why the outer belt electron decay is independent of pitch angle but dependent upon energy. This implies that satellite observations can reveal local pitch angle diffusion rates, themselves intimately connected with the wave properties. Thus, a connection is made between observed wave properties and observed/computed scattered electron flux, consistent with theory. Regions where the flux is pitch angle dependent are isolated in the low-energy slot region where we show that the real shape is a smoothed version of the ideal top-hat distribution computed from theory. The impact of this work is improved understanding of the belt evolution for space weather prediction, with a proposed event-driven method that accurately (within ×2) predicts the electron flux decay after storms.

1. Introduction

The dynamics and physical morphology of the electron radiation belts during the month of March 2013 have been subject to much attention in the recent literature (e.g., Baker et al., 2014; Hudson et al., 2015; Xiao et al.,

2014; W. Li, et al., 2014; Z. Li, et al., 2014; Boyd et al., 2014; Yu et al., 2014; Brito et al., 2015; Reeves et al., 2015; Shprits et al., 2015; Ma et al., 2016, 2017; Ripoll, Loridan et al., 2016; Ripoll et al., 2017). Our current study is focused on a global characterization of the fast slot formation and the outer belt decay from 4 to 15 March 2013, which led to a drastic reduction in the flux level of the radiation belts, for L-shells between $L \sim 2$ and $L \sim 5$ and for kinetic energy, E, between 100 keV and a couple of MeV. Understanding (and predicting) the physical mechanisms that control such a flux reduction in the heart of Earth's radiation belts is critical to preserve orbital hardware that operates in the region. We analyze the evolution of the full three-dimensional (3D) structure of the radiation belts in L, E, and equatorial pitch angle, α_0, during quiescent days between storms on 1–17 March. Computations are made both with a one-dimensional (1D) reduced Fokker-Planck (1D-RFP) model and with the Versatile Electron Radiation Belt (VERB-3D) code (e.g., Drozdov et al., 2015; Kim et al., 2011; Subbotin et al., 2010, 2011; Subbotin & Shprits, 2009), which is based on a full 3D Fokker-Planck formalism. Event-specific electron lifetimes and pitch angle diffusion coefficients are used respectively in each code (Ripoll, Loridan et al., 2016; Ripoll et al., 2017). Observations from the Magnetic Electron and Ion Spectrometer (MagEIS) instrument on board Van Allen Probe A are used to validate the model results.

The storm of 1 March 2013 is associated with a high-speed solar wind stream that created strong erosion of the plasmasphere and resulted in outer belt flux dropout events followed by enhancements of relativistic electrons in the slot region and outer belt. Three days after this storm, an extended period of 11 days of quiet solar wind conditions persisted, with the plasmasphere expanding outward to $L \sim 5.5$, and radial transport and gradual particle loss throughout the 11 days. Ripoll, Loridan et al. (2016), Ripoll et al., (2017) showed this electron depletion occurs in both the slot region and the outer belt and is essentially related to atmospheric loss due to pitch angle scattering from whistler mode hiss waves. The demonstration was made by using observed wave properties to develop "event-specific" pitch angle diffusion coefficients to calculate flux decay. The authors studied the radiation belt dynamics with a 1D-RFP model, reproducing the characteristic quiet time S-shape to the inner boundary of the outer belt when drawn in the (L, E) plane (Reeves et al., 2015; Ripoll, Loridan et al., 2016; Ripoll, Reeves et al., 2016; Ripoll et al., 2017). These prior studies were unable to address the pitch angle dependence of the flux evolution, while the present work produces for the first time a global analysis of the 3D (L, E, α_0) structure of the radiation belts during the quiet times from 4 to 15 March and compares the model output to pitch angle-resolved observations.

In the current study we present the 1D and 3D models used for the simulations in sections 2 and 3, respectively; describe and discuss MagEIS observations of the 4–15 March event in (t, L, E, α_0) in section 4; present the numerical results and provide the analysis of the radiation belts structure in section 5; discuss more particular features of the radiation belts structure in section 6; and use dedicated error metrics to quantify the accuracy of both the 1D and 3D models in section 7. Section 8 summarizes our findings and conclusions.

2. Fokker-Planck Modeling of the Radiation Belts

The time evolution of the gyro-, bounce-, and drift phase-averaged phase space density (PSD), $f(t, L, \mu, K)$, in the presence of radial and pitch angle diffusion can be described by the following (Schulz & Lanzerotti, 1974; Shprits et al., 2008):

$$\frac{\partial f}{\partial t} = L^2 \frac{\partial}{\partial L}\bigg|_{\mu,K} \left(\frac{D_{LL}}{L^2} \frac{\partial f}{\partial L}\bigg|_{\mu,K} \right) + \frac{1}{G} \frac{\partial}{\partial \alpha_0}\bigg|_{L,E} \left(G D_{\alpha_0 \alpha_0} \frac{\partial f}{\partial \alpha_0}\bigg|_{L,E} \right) + \frac{1}{p^2} \frac{\partial}{\partial p}\bigg|_{L,\alpha_0} \left(p^2 D_{pp} \frac{\partial f}{\partial p}\bigg|_{L,\alpha_0} \right) - \frac{f}{\tau_b} \tag{1}$$

with $G = T(\alpha_0) \sin(2\alpha_0)$, μ the first adiabatic invariant, and K proportional to the second adiabatic invariant, J ($K = J\sqrt{B_m}/2p$, with B_m the mirror point magnetic field and p the electron momentum). In this article, $L = L^*$ with L^* the Roederer L-shell value (Roederer, 1974). D_{LL} is the radial diffusion coefficient, $D_{\alpha_0 \alpha_0}$ is the bounce- and drift-averaged equatorial pitch angle diffusion coefficient, and $T(\alpha_0)$ is proportional to the bounce period in a dipole magnetic field evaluated at the equatorial pitch angle, α_0. τ_b is the electron lifetime within the loss cone, $\tau_b = 0.25T(\alpha_0)$ for $\alpha_0 \leq \alpha_{lc}$ and $1/\tau_b = 0$ elsewhere. Equation (1) neglects off-diagonal terms in the diffusion tensor. VERB-3D is used to solve equation (1) (e.g., Kim et al., 2011; Shprits et al., 2009; Subbotin et al., 2010, 2011). VERB-3D uses an implicit finite differences method and an operator-splitting technique between radial and local processes. A dipole magnetic field is used in equation (1) to compute the magnetic invariants at which the PSD is evaluated when converting from flux to PSD.

Verifications and validations of VERB-3D have been published (e.g., Aseev et al., 2016; Subbotin & Shprits, 2009). Additionally, here we have verified pitch angle diffusion (with the diffusion coefficients of this work that are presented later) by comparing successfully VERB-3D solutions with the ones of a second code (Réveillé et al., 2001; Ripoll & Mourenas, 2012; not shown). The grid is composed of 45 uniformly distributed bins in L-shell, from $L = 1.6$ to $L = 5.5$. The grid at $L = 5.5$ is composed of 100 uniformly distributed pitch angle, from $0.3°$ to $89.7°$, and 100 uniformly distributed in $\log_{10}$ space bins in energy from 0.5 keV to 4.5 MeV. The radial diffusion term is solved on the (μ, J, L) grid, while local diffusion term is solved on the (energy, α, L) grid. The values of μ and J are the same at all nodes along L. At each L, the values of energy and pitch angle are calculated from (μ, J, L) and the PSD is interpolated onto the (energy, α, L) grid after solving the radial diffusion (see details in Subbotin and Shprits, 2009).

When pitch angle diffusion is fast relative to radial diffusion, there exists an equilibrium pitch angle distribution that decays exponentially at a time-independent rate, τ, the electron lifetime. In this case, equation (1) reduces to

$$\frac{\partial f}{\partial t} = L^2 \frac{\partial}{\partial L}\bigg|_{\mu,K} \left(\frac{D_{LL}}{L^2} \frac{\partial f}{\partial L}\bigg|_{\mu,K} \right) - \frac{f}{\tau}\bigg|_{L,E} \tag{2}$$

which is a 1D-RFP equation (Walt, 1970) that solves for the PSD in the presence of radial diffusion and losses from wave scattering (Lyons & Thorne, 1973; see also derivation in Ripoll, Reeves et al., 2016). Equation (2) neglects energy diffusion. In equation (2) loss is produced by a mean rate (τ), while in equation (1) electrons pitch angle diffuse until they are eventually lost at the loss cone pitch angle (α_{lc}), where the mirror point reaches the high-density atmosphere near 100-km altitude.

In the 1D-RFP model we use both a dipole and the T89 (Tsyganenko, 1989; nondipole) magnetic field model to compute magnetic invariants in the flux-PSD extrinsic conversion that is required for data preprocessing (transformation from the observed flux to PSD in order to feed the Fokker-Planck equation with one initial condition and two boundary conditions) and postprocessing (transformation of the calculated PSD into fluxes). The intrinsic conversion between magnetic invariants and physical variables made in equation (2) in order to define $\tau(E, L)$ at fixed (μ, K) is also performed with either a dipole or the T89 magnetic field models. The 1D-RFP code we use here has been used successfully numerous times (Ripoll, Loridan et al., 2016; Ripoll, Reeves et al., 2016; Ripoll et al., 2017), and it reproduces analytical solutions (Loridan et al., 2017). A novel aspect of this work is to solve equation (2) with respect to all K (and not only $K = 0$ since τ is independent of K). The K dependence of the solution comes here from the initial and boundary conditions essential to accurately compute the full dynamics and ultimately the omnidirectional flux. The grid is composed of 200 μ from 0.45 MeV/G to 15,770 MeV/G (uniformly distributed in $\log_{10}$ space) and of 100 K from 10^{-3} to 10^3 G$^{1/2}$Re (uniformly distributed in $\log_{10}$ space).

Both the 1D-RFP code and VERB-3D use the Ozeke et al. (2014) ultralow-frequency wave-driven statistical radial diffusion coefficient, since this model had the greatest accuracy among the other four models for this event (Ripoll et al., 2017). Instantaneous D_{LL} derived from the Canadian Array for Real-time Investigations of Magnetic Activity (CARISMA) magnetometer array database were found to be consistent with the Ozeke et al. (2014) statistical D_{LL} model. Possible deviations from purely diffusive transport (e.g., Ukhorskiy & Sitnov, 2008, 2012) are ignored.

3. Pitch Angle Diffusion Coefficient and Electron Lifetime

The calculation of the pitch angle diffusion coefficients, $D_{\alpha_0 \alpha_0}(L, E, \alpha_0)$, is based on the observed, spatially and temporally resolved wave properties of hiss waves (0.05–2 kHz; e.g., Santolik et al., 2001) as well as plasma density (Kurth et al., 2015; Thaller et al., 2015) measured from the Electric and Magnetic Field Instrument Suite and Integrated Science (EMFISIS) Waves instrument on board the Van Allen Probe A spacecraft (RBSP A; Kletzing et al., 2013). Consistency between plasma density and hiss wave amplitudes is essential to reach good accuracy in radiation belts simulations (Malaspina et al., 2017; Malaspina et al., 2018; Ripoll et al., 2017). The method of computation is described in Ripoll et al. (2017) and shall not be repeated here. The calculation of the pitch angle diffusion coefficients accounts for all necessary harmonics and both wave normal angle and pitch angle dependence. Both the low-frequency and dense-plasma approximations (Albert, 1999,

2005; Lyons et al., 1972) are used. Code validation is described in Réveillé et al., (2001), Ripoll, Albert et al. (2014), and Ripoll and Mourenas (2012). We made use of the mean wave normal angle width, $\Delta\theta_m(t, L)$, which is derived from the EMFISIS data (Santolík et al., 2003). Variation of the wave properties with latitude is not accounted for (cf. discussion in Ripoll et al. (2017). Magnetic Local Time (MLT) dependence of the wave amplitude is accounted for (Spasojevic et al., 2015). These diffusion coefficients are combined with VERB-3D in order to define what we may generically refer to hereafter as a 3D Fokker-Planck model.

Our analysis starts on 4 March when calm conditions prevail. The plasmasphere extends to $>L = 5.5$ from 4 to 16 March and justifies the use of only plasmaspheric hiss waves to compute the pitch angle diffusion coefficient as chorus waves are typically only observed outside the plasmasphere. Lightning-generated (LG) waves and very low frequency (VLF) transmitter waves that can have some effects in the plasmasphere (e.g., Abel & Thorne, 1998) are neglected based on their low mean amplitude relative to hiss (e.g., Ma et al., 2017).

Diffusion coefficients are computed and time averaged from 4 to 10 March and 11 to 15 March. We break up the 11 days into these two intervals to better account for the wave variability (cf. Figure 8 of Ripoll et al. (2017). Electron lifetimes in equation (2) and pitch angle diffusion coefficients in equation (1) are related to each other by a closed-form expression (e.g., Albert, 1994, 1999; Lyons et al., 1972; Ripoll, Chen et al., 2014; Ripoll, Loridan et al., 2016; Ripoll, Reeves et al., 2016, 2017) that is used to self-consistently compute the lifetime. Both are plotted in Figure 1. The mean power is used in the simulations as is commonly done (e.g., Meredith et al., 2014). Following Watt et al. (2017), we have checked that results are similar when the median power, $\widetilde{B^2}$, is used instead of the mean power, $\overline{B^2}$, with $\overline{B^2}/\widetilde{B^2}$ varying in time and L-shell but equal on average to $\sim(1.4)^2$. The region of strongest diffusion follows a diagonal line such that maximum pitch angle diffusion occurs at lower energy as L increases. This diagonal line shifts up toward higher energy as pitch angle increases. Electron lifetimes follow a similar mean diagonal line of minimal value.

An important property that will be discussed later should be noticed in Figure 1; the pitch angle diffusion coefficients are homogeneous with respect to pitch angle for $L > \sim3.5$, $E > \sim100$ keV, and $\alpha_0 \sim <60°$. Such a shape is similar to the diffusion coefficients of 200-keV electrons in Figure 4 of Lyons et al. (1972; see also Figure 1 in Albert, 1994), occurring here systematically above 100 keV. One reason is that we use ±50 harmonics to compute $D_{\alpha_0\alpha_0}(L, E, \alpha_0)$, whereas ±5 harmonics were used in Lyons et al. (1972). Use of only a small number of harmonics creates gradients with respect to α_0 in the diffusion coefficients at relativistic energies. Another reason is that wave properties strongly influence the homogeneity of the pitch angle diffusion coefficient; large frequency width ($>\sim600$ Hz) and relatively small ($\sim<45°$) wave normal angle width favor the homogeneity. As a consequence, the diffusion coefficients end up homogeneous, and Figure 1 shows that $D_{\alpha_0\alpha_0}(\alpha_0\sim[25°, 60°])\sim D_{\alpha_0\alpha_0}(\alpha_{0,LC})\sim1/\tau$.

4. MagEIS Observations

Figure 2 shows flux observations on outbound orbits from 4 to 15 March from the MagEIS instrument (Blake et al., 2013) on board RBSP A. The Level 2 (L2) spin-averaged MagEIS-measured flux (integrated over solid angle; first column); omnidirectional Level 3 (L3) MagEIS-computed flux (second column), noted thereafter as J_{omni}^{RBSP}; and directional L3 MagEIS-measured flux (third to seventh columns), noted thereafter as J^{RBSP}, are represented. The Roederer L-shell value is computed with the use of the T89 magnetic field model. The data grid is made of 800 available L-shells from $L = 1.6$ to $L = 6.1$, 20 available energies from 30 keV to 4.2 MeV, and 11 available pitch angles from 8° to 172°. Data have been background corrected (Claudepierre et al., 2015) and interpolated onto a fixed (L, E) grid that matches the simulation grid used in the next section.

The L3 omnidirectional flux (second column) is computed here from the sampled background-corrected MagEIS L3 directional fluxes measured at local pitch angles $\alpha = 8°, 25°, 41°, 57°, 74°, 90°, 106°, 123°, 139°, 155°, 172°$ that are symmetrized by direct averaging to be sampled at $\alpha = 8°, 25°, 41°, 57°, 74°, 90°$ and integrated with respect to α and solid angle in order to provide a local omnidirectional flux at the latitude of the Van Allen Probes. This requires a directional flux function defined at every α that is generated by linear interpolation (or extrapolation when data are lacking). Both background-corrected L2 spin-averaged flux integrated with respect to solid angle (used in Ripoll, Loridan et al., 2016; Ripoll et al., 2017) and L3 omnidirectional flux are very close to each other, demonstrating successful measurement and numerical reconstruction, plus the capacity of this spin-averaged measurement to well approximate the omnidirectional fluxes.
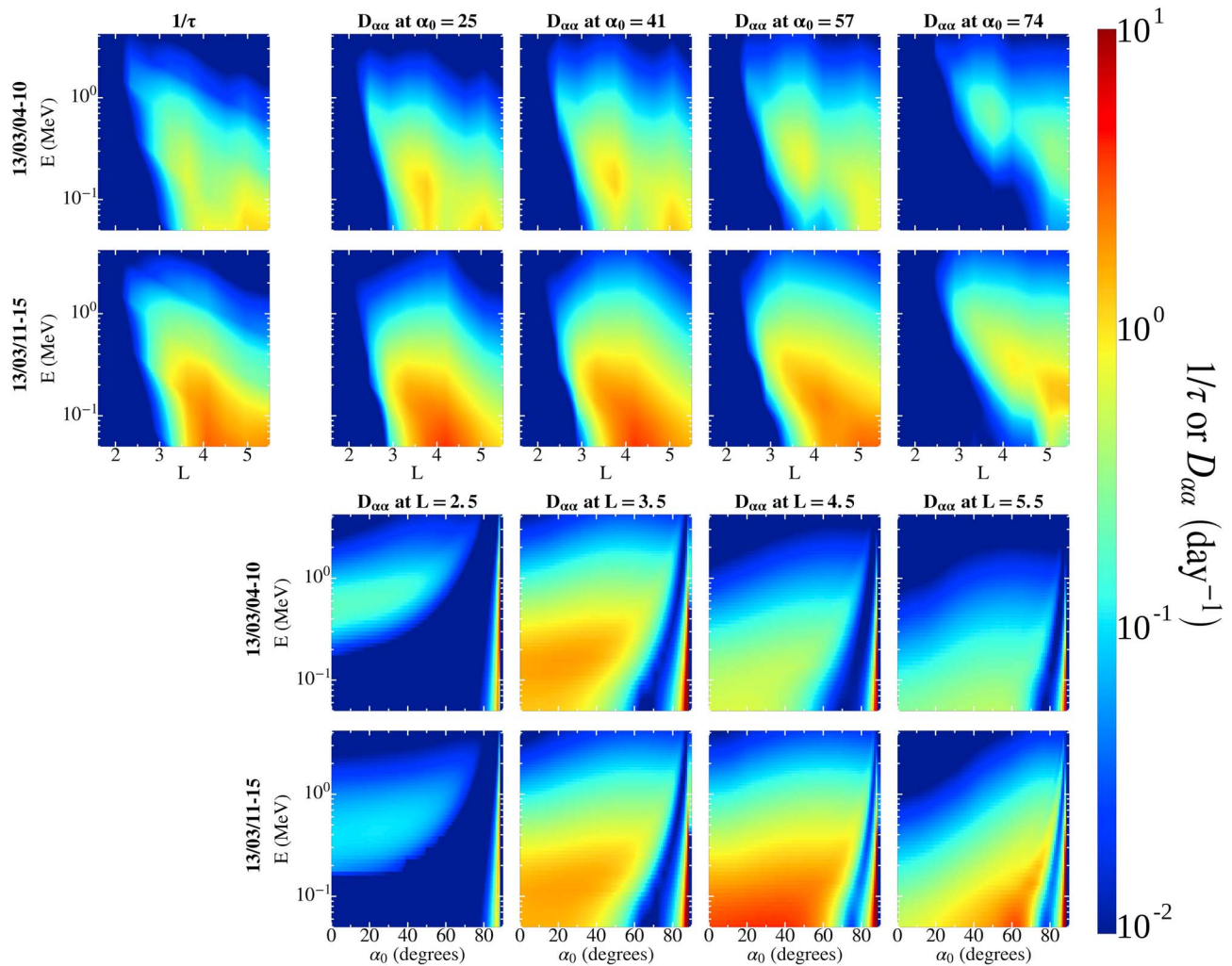
Figure 1. (first two rows, first column on the left) Inverse of the electron lifetime and (second to fifth columns) equatorial pitch angle diffusion coefficient at $\alpha_0 = 25°$, 41°, 57°, and 74° in days^{-1}. They are computed (first raw) from 4 to 10 March and (second raw) from 11 to 15 March 2013. (second to fifth columns) diffusion coefficients are computed from n cyclotron harmonics resonances and Landau resonance. (third and fourth rows) The diffusion coefficients plotted versus (E, α_0) for (first to fourth columns) $L = 2.5$, 3.5, 4.5, 5.5. This figure shows the diffusion coefficients are quite homogeneous for $\alpha_0 \sim < 60°$, $E > 100$ keV, $3.5 < L < L_{pp} \sim 6$, and we have $D_{\alpha_0\alpha_0}(\alpha_0 \tilde{} [25°, 60°]) \tilde{} D_{\alpha_0\alpha_0}(\alpha_{0,LC}) \tilde{} 1/\tau$, which explains the homogeneous outer belt structure illustrated in Figure 2.

Symmetrized directional fluxes are used in the simulations as initial conditions and boundary conditions at $L = 1.6$ and $L = 5.5$ and for validation. Since the Van Allen Probes magnetic latitude can be as high as 20°, the local 90° pitch angle represents a maximal equatorial pitch angle, α_{0max}, as low as ~55° at $L = 1.6$, ~70° at $L = 3.5$, and ~80° at $L = 4.5$. Therefore, a linear extrapolation of the log$_{10}$ of the local measured symmetrized directional flux is performed in Figure 2 from $\alpha_{0max}(L)$ to 90°.

Figure 2 (second column) shows a daily dynamic enlargement of the slot region and a decrease in the flux level in the outer belt. The creation of the slot is fast and achieved in 10 days (omnidirectional flux level reduced by 1–2 orders of magnitude depending on the location and energy). In turn, the outer belt flux decays also gradually and falls by a factor ~20. The decay creates an energy structure with an S-shaped edge of the outer belt (Reeves et al., 2015; Ripoll, Loridan et al., 2016; Ripoll, Reeves et al., 2016; Ripoll et al., 2017).

The pitch angle-resolved data show a structure in energy and L-shell that is quite similar to the omnidirectional fluxes. The decay of the outer belt is quite uniform across pitch angles, with only small differences in the structure at different pitch angles (due to the rather isotropic injection). Outer belt directional fluxes are nearly isotropic (by a factor of ~2) at any given time. The quasi-invariance of the directional
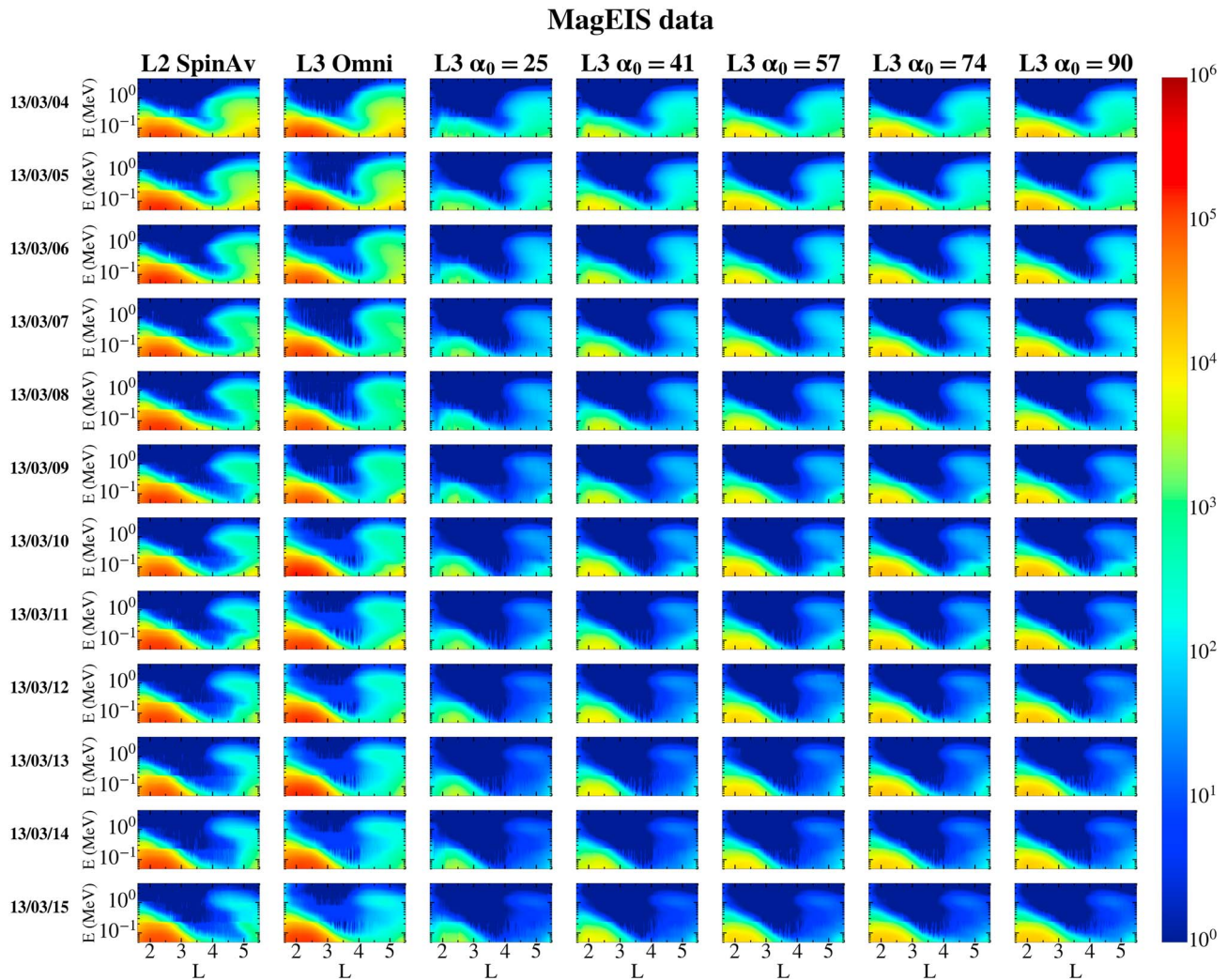
Figure 2. (first column on the left) MagEIS Level 2 (L2) spin-averaged flux (integrated over solid angle and in the unit of #·cm^{-2}·s^{-1}·keV^{-1}) in the (L, E) plane from 4 to 15 March 2013 compared with (second column) the Magnetic Electron and Ion Spectrometer (MagEIS) Level 3 (L3) omnidirectional flux (#·cm^{-2}·s^{-1}·keV^{-1}) computed by integration of the (third to seventh columns) L3 MagEIS local directional symmetrized flux (#·cm^{-2}·sr^{-1}·s^{-1}·keV^{-1}) projected at α_0 = 25°, 41°, 57°, 74°, 90°.

outer belt flux with pitch angle is remarkable and occurs at all energy. It is consistent with the absence of local acceleration. Likewise, the position of the inner edge of the outer belt is relatively independent of pitch angle.

In contrast, the inner belt and the inner slot edge are strongly pitch angle dependent. The inner belt is wider at large pitch angle, leading to a narrower slot and to an outer edge of the inner belt increasing in L as pitch angle increases. The highest flux in the inner belt occurs at large pitch angle (for $E < 900$ keV; Fennell et al., 2015). At 200 keV and $L = 1.6$, directional inner belt fluxes are ~50 times higher at large pitch angle than at small pitch angle. This ratio decreases with increasing energy, still remaining a factor ~10 at ~600 keV. At $L = 1.5$, flux above 10^3 #·cm^{-2}·sr^{-1}·s^{-1}·keV^{-1} corresponds to energies of ~<200 keV at $\alpha_0 = 25°$, ~<400 keV at $\alpha_0 = 57°$, and ~<600 keV at $\alpha_0 = 90°$. Hence, the inner belt is primarily made up of a large pitch angle (nearly equatorial, ~perpendicular) population for all $E < 900$ keV and of a small pitch angle population (~field-aligned) only at lower energies (a couple of hundred keV). At lower energy (~<100 keV), enhancements associated with substorm activity are intermittent (e.g., Turner et al., 2015; Zhao et al., 2017). They replenish the low-energy high-flux zone of the inner belt below ~100 keV at all pitch angles on 10 March.

5. Numerical Results

Figures 3 and 4 show the results of the two simulation methods used in this work at the resolution of 1 day and for all available pitch angles ($\alpha_0 > \alpha_{0lc}$) for direct comparison with the MagEIS data (Figure 2). Figure 3
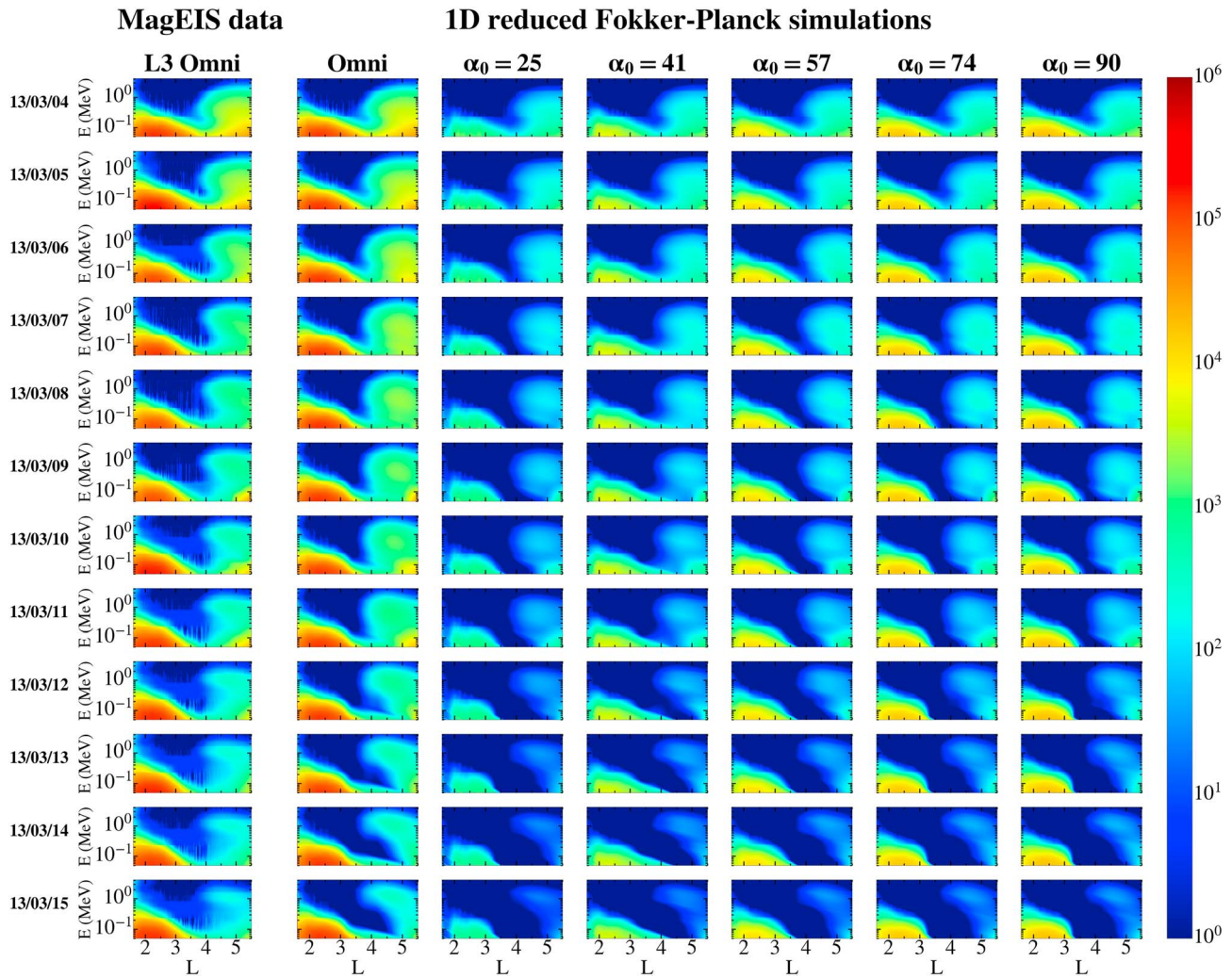
Figure 3. Comparison between (first column on the left) Magnetic Electron and Ion Spectrometer (MagEIS) omnidirectional flux (#·cm^{-2}·s^{-1}·keV^{-1}) computed from Level 3 (L3) MagEIS data (cf. Figure 2) and (second column) the omnidirectional flux (#·cm^{-2}·s^{-1}·keV^{-1}) computed from reduced Fokker-Planck (1D-RFP) simulations in the (L, E) plane from 4 to 15 March 2013 during quiet times. The 1D-RFP simulated omnidirectional flux is computed from all simulated directional fluxes at the latitude of the spacecraft. The third to seventh columns show the equatorial directional flux (#·cm^{-2}·sr^{-1}·s^{-1}·keV^{-1}) at selected α_0 = 25°, 41°, 57°, 74°, 90° for comparison with the observations provided in Figure 2.

(columns 2 to 7) shows the 1D-RFP simulations, and Figure 4 (columns 2 to 7) shows the VERB-3D simulations. Both initial and boundary conditions are taken from MagEIS L3 unidirectional fluxes, respectively at $t = 0$ at all L-shells and at $L = 1.6$ and $L = 5.5$. Boundary conditions are supplied when RBSP A is at $L = 5.5$ (each ~9 hr), interpolated between two passes, and updated every 3 hr in the codes. Simulated omnidirectional fluxes, J_{omni}^{simu}, are computed with respect to equatorial pitch angle (Roederer & Zhang, 2014). The computation method is the same for both observed (cf. section 4) and simulated omnidirectional fluxes. Electrons with pitch angles that are too large to allow them to reach the spacecraft are not counted in the omnidirectional flux. The latter is indeed calculated, for each day of the simulation, at the local latitude of RBSP A, which is L dependent.

MagEIS L3 omnidirectional fluxes of Figure 2 (second column) are repeated in Figures 3 and 4 (first column) to facilitate cross-comparisons with the simulated omnidirectional fluxes next to them (second column). The simulated omnidirectional flux agrees with the observed omnidirectional flux, with a characteristic boundary to the outer belt that has been described as "S-shaped" in energy and L. Figures 3 and 4 show a similar structure of the simulated omnidirectional flux (second column) that is well restituted by both 1D and 3D models. Differences were found to be minor between the 1D solution computed with T89 and the 1D solution computed with a dipole field. There is no significant effect found of the magnetic field topology from 4 to 15
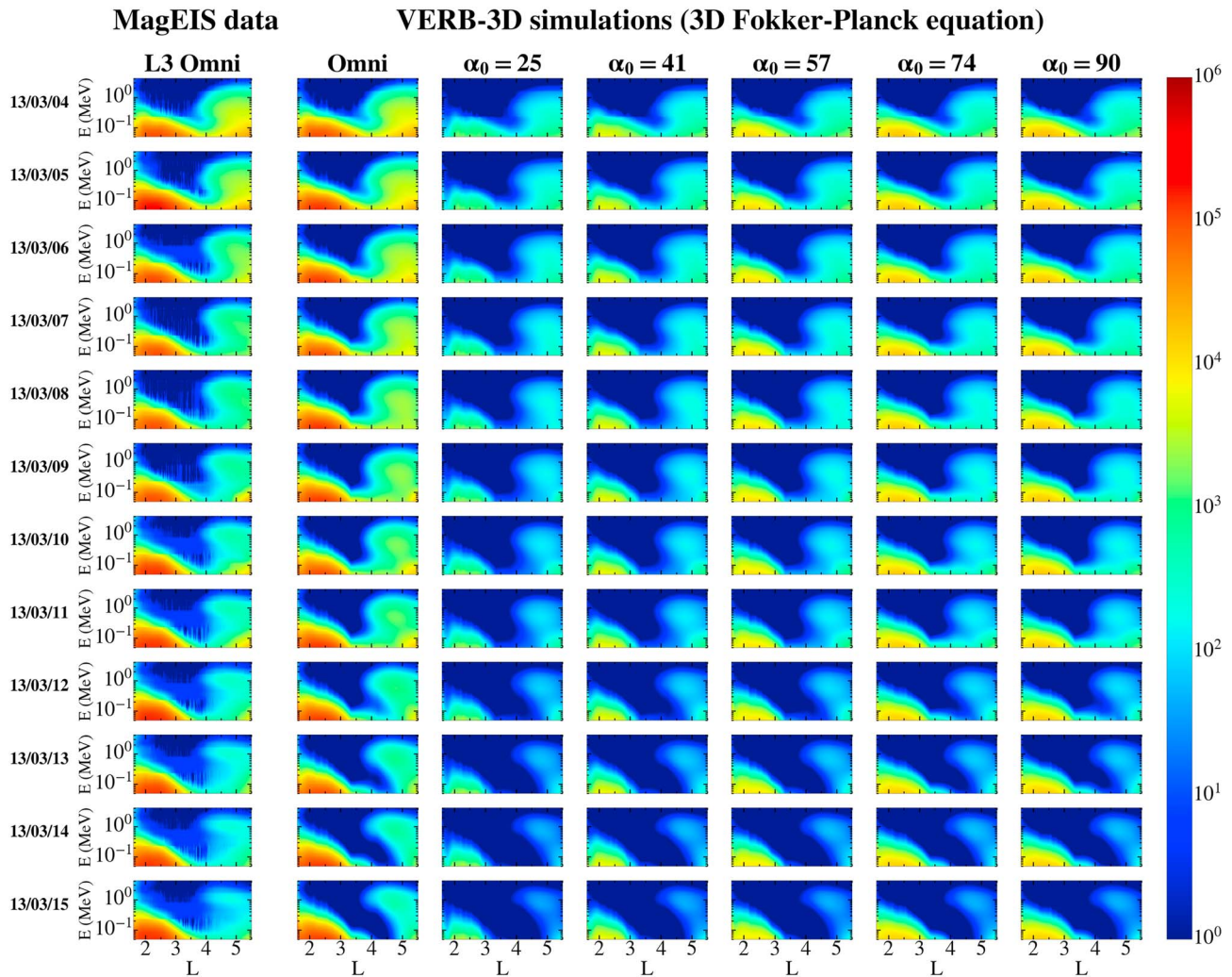
Figure 4. Comparison between (first column on the left)) Magnetic Electron and Ion Spectrometer (MagEIS) omnidirectional flux (#·cm^{-2}·s^{-1}·keV^{-1}) computed from Level 3 (L3) MagEIS data (cf. Figure 2) and (second column) the omnidirectional flux computed with Versatile Electron Radiation Belt (VERB-3D) in the (L, E) plane from 4 to 15 March 2013 during quiet times. The omnidirectional flux is computed from all simulated directional fluxes at the latitude of the spacecraft. The third to seventh columns show the equatorial directional flux (#·cm^{-2}·sr^{-1}·s^{-1}·keV^{-1}) at selected α_0 = 25°, 41°, 57°, 74°, 90° for comparison with the observations provided in Figure 2.

March 2013. This is due to the quiet time nature of the magnetosphere during that time period, which appears through low daily Kp values ($Kp < 2$) and to an extended stable plasmasphere up to the boundary conditions of the simulation ($L \leq 5.5$). With these conditions ($L \leq 5.5$ and $Kp < 2$), the T89 model does not depart significantly enough from a dipole field so that it would change the predicted fluxes.

Simulations are not in perfect agreement with the observations, but the overall trend is very good. At $E \sim 200$ keV, the slot width after 11 days is $\Delta L \sim 2$, spreading over from $L \sim 3$ to $L \sim 5$ in both simulations and observations. The greatest inaccuracies occur below 100 keV due to the absence of modeling of the low-energy injections. Daily intensifications on 9–10 March are not reproduced by the models. The coincident location of the observed slot and the diagonal of maximal diffusion is clear, with the location of a bite-out for L in [4.7, 5.2] and E in [200, 500] keV in both simulations and observations. Simulations overestimate the flux (for both 1D and 3D models), causing a larger spread over energy, from 0.5 to 2 MeV. The upper part of the S-shaped outer belt is a remarkably dense pocket of core electrons located at L in [4, 5.2] and E in [0.7, 2] MeV that is preserved due to weaker pitch angle diffusion. The lower-energy (<200 keV) electrons in the outer belt have been described as the radiation belt "seed population" and the higher energies as the "core" radiation belt (e.g., Boyd et al., 2014; Jaynes et al., 2015). Here we see that the seed population and the core population are distinct and frequently separated by a bite-out of low fluxes at intermediate energies (~200–500 keV),

particularly at L-shells from 4.7 to 5.2. Simulations over a longer period show full depletions of the electrons in this in-between zone (L in [4.7, 5.2] and E in [200, 500] keV) as soon as the outer inward flux is weak enough not to replenish it. Such conditions create an outer belt double structure only made of the low-energy seed electrons (below ~100 keV for $L > 5$) and the isolated pocket above ~0.7 MeV for $L > ~4.5$ with nothing in between (not shown). Such a structure with a unique denser pocket was observed in (Reeves et al., 2016, Figure 12D). Observations show that the low-energy seed electrons can penetrate down to low L-shells where they merge with the low-energy inner belt (Reeves et al., 2016; Turner et al., 2015, 2016; Lejosne et al., 2018). Finally, outward radial diffusion causes significant flux decay only above $L \sim 5.2$, based on the gradual flux decay occurring for energies that are too high for significant hiss loss in ~10 days.

Figure 5 combines results of Figures 2–4, all together at a lowest temporal resolution of 4 days and at only three selected pitch angles. This provides a more synthetic view of all the results and facilitates comparisons between them. Simulated unidirectional flux (J^{simu}) snapshots follow the observed dynamics. The flux decay is slower from 4 to 10 March than from 11 to 15 March due to the pitch angle diffusion coefficients of Figure 1 that are significantly different for each of the two periods. This leads to a slightly overestimated outer belt on 10 March, better resolved with VERB-3D. Unidirectional outer belt fluxes are quasi-isotropic in pitch angle, with slightly lower flux at small pitch angles in both simulations and observations. This is explained by the diffusion coefficients that are quasi-homogeneous with respect to pitch angle for $L > 3.5$, $E > 100$ keV, and $\alpha_0 \sim <60°$ (Figure 1). In Figure 5 (identically in Figures 3 and 4), both 1D and 3D solutions agree well, with differences hardly visible, for two main reasons. First, the data-based initial condition allows the simulation to start with the correct solution (in both models). Second, the homogeneity property of the diffusion coefficients for $\alpha_0 \sim <60°$ leads to $D_{\alpha_0\alpha_0}(\alpha_0 \tilde{} [25°, 60°]) \tilde{} 1/\tau$. An illustration of this property is, for instance, brought by the 25° unidirectional fluxes that decay similarly in Figures 5. Therefore, the electron lifetime becomes an excellent description of the loss rate for all pitch angles below $\alpha_0 \sim 60°$. Above $\alpha_0 \sim 60°$, for which $D_{\alpha_0\alpha_0}$ and $1/\tau$ differ more, 3D and 1D solutions will produce different evolution of the flux, with a degradation of the solution accuracy increasing in time with the 1D model. This is not visible at the spatial and temporal scales of Figures 3–5, indicating the error does not build up significantly in 11 days. The main differences between the small pitch angle ($\alpha_0 \sim <60°$) and the large pitch angle ($\alpha_0 \sim >60°$) appear through the slot width, which is larger at low pitch angle ($\Delta L \sim 2$) and smaller otherwise ($\Delta L \sim 1.5$; cf. Figures 3–5). Error metrics (Morley, 2016; Brito & Morley, 2017) are used in section 7 to quantify quantitatively the evolution of the error and the accuracy of each model.

In contrast, the simulated inner belt is pitch angle dependent. Neither the diffusion coefficients (at all α_0) nor the inverse lifetime is large enough in the simulations for $L \sim [1.5, 2.2]$ and $E \sim [50, 900]$ to produce changes (particularly in 11 days). This preserves the inner belt core from fast hiss effects. Only its outer edge varies in the simulations as in the observations. The absence of observed significant decay inside the inner belt (>100 keV) implies waves of higher frequency than hiss, for example, VLF transmitter or LG waves, do not have a large amplitude, justifying our previous assumption. Otherwise, these waves would scatter inner belt electrons (e.g., Abel & Thorne, 1998; Albert, 1999; Ripoll, Albert et al., 2014; Shprits et al., 2008). Here their presence and weakness is confirmed from EMFISIS observations. Only at the scale of months and years can these waves have an effect and contribute with hiss to create a stable pitch angle-dependent low-energy inner belt core dominated by a large pitch angle population. This implies a total diffusion coefficient with first negative cyclotron harmonic ineffective (or less effective) from moderate to high pitch angle electrons below $L = 2$. Thus, the overall inner belt structure, which is determined by the initial condition, is stable at small timescales of tens of days and variable over longer timescales. Over timescales of months the weaker effects of pitch angle scattering from hiss, as well as VLF transmitter or LG waves, begin to dominate the decay rates for inner-zone electrons.

6. Homogeneous Outer Belt Flux, Bottleneck-Shaped Distributions, and Equilibrium Structure

The homogeneity property of the diffusion coefficients (for $L > ~3.5$, $E > 100$ keV, and $\alpha_0 \sim <60°$ and consequently of the outer belt flux) has three important consequences. First, it signifies that pitch angle equilibrium (e.g., Lyons et al., 1972; i.e., a homogeneous steady decay at all pitch angles) is indeed reached quasi-instantaneously for the most dynamic small pitch angle electron population. Full pitch angle equilibrium
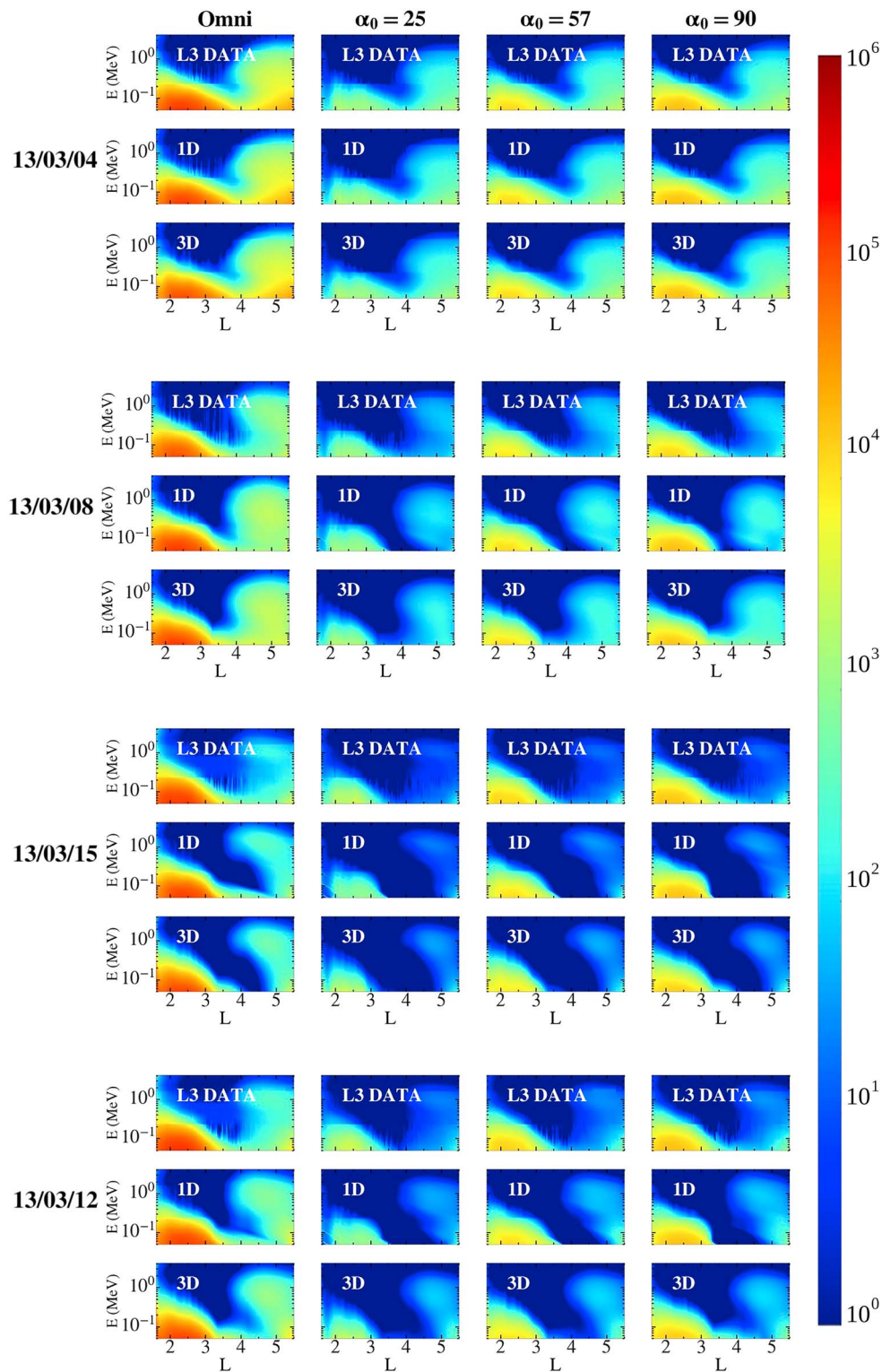
Figure 5. (top to bottom) Four daily panels showing the evolution of the flux (first to fourth columns) in the (L, E) plane on the 4, 8, 12, and 15 of March 2013. (first column) The omnidirectional flux (in $\#\cdot cm^{-2}\cdot s^{-1}\cdot keV^{-1}$) is the integral of the directional flux with respect to pitch angle and solid angle, shown here at (second to fourth columns) $\alpha = 25°, 57°, 90°$ (in $\#\cdot cm^{-2}\cdot sr^{-1}\cdot s^{-1}\cdot keV^{-1}$). In each panel we compare (first line) the Magnetic Electron and Ion Spectrometer (MagEIS) data, (second line) the 1D reduced Fokker-Planck (1D-RFP) results (1D), and (third line) the Versatile Electron Radiation Belt (VERB-3D) results (3D). The 1D-RFP and VERB-3D results are plotted at the latitude of the spacecraft. Notable results in these figures are the pitch angle-dependent inner belt flux decay, a more homogeneous flux decay in the outer belt with two distinct (L, E) regions (seed electrons below $\sim$<100 keV and a core radiation belt population for $L \sim [4.5, 5.5]$ and $E \sim [0.7, 2]$ MeV) and the agreement of 1D and 3D simulations with observations.

for all [α_{lc}, 90°] requires longer timescales. Second, the homogeneity of pitch angle diffusion leads to a homogeneous flux decay that cannot present a bottleneck-shaped distribution (also called top-hat distribution) with respect to pitch angle (e.g., Lyons et al., 1972). Here both observations and simulations agree on the absence of a bottleneck-shaped distribution in the outer belt. (Conditions for which the bottleneck-shaped distribution occurs are discussed below.) Conversely, the more the distribution is bottleneck shaped, the more the pitch angle diffusion coefficient gradient regions have to be important. The fact that 3D simulations produce a homogeneous structure of the outer radiation belt, in agreement with observations, suggests that (1) homogeneous pitch angle diffusion coefficients are appropriate; (2) the daily wave properties that led to such homogeneous diffusion coefficient are consistent and adequate; and (3) conversely, the observed decay rate of the unidirectional flux reveals both the local pitch angle diffusion rate and apparent lifetime (associated with the dynamics of the small pitch angle population, i.e., $\alpha_0 \sim$ <60°). The latter property can lead to the direct determination of empirical decay rates from observations and has great potential implications in the way we relate wave properties to the pitch angle diffusion rates.

The distribution function versus equatorial pitch angle plotted in Figure 6 tells us more on pitch angle-dependent decay rates and whether or not the well-known bottleneck-shaped distribution occurs (e.g. Abel & Thorne, 1998; Albert, 2012; Gao et al., 2015; Lyons et al., 1972; Meredith et al., 2009; Ni et al., 2013, 2014; Selesnick et al., 2013). We find the bottleneck distribution is not as distinct in the observations as in our simulations. In the observations, a strong gradient (a few orders of magnitude) in pitch angle is observed in the distribution at some (L, E) where the simulations show the bottleneck-shaped distribution. Such a steep gradient is indeed observed in the data for (L, E) but only where the following six conditions are fulfilled: (1) the diffusion coefficient presents a well-marked bottleneck with a largely spread gradient region between low and high pitch angles; (2) newly injected electrons from inward radial transport do not mask pitch angle scattering; (3) dynamics is fast enough to cause observable decays over a few orders of magnitude (over ~10 days); (4) electron levels are not close to background levels; (5) pitch angle resolution is high enough; and (6) the latitude of the spacecraft is low enough to allow observations of high pitch angle electrons. Conditions 1 and 3 are associated with the diffusion coefficients and therefore with wave and plasmasphere properties. While 1 and 3 are frequent enough in terms of (L, E), it seems the width of the region with small diffusion in pitch angle between cyclotron and Landau harmonics has to be large in order to produce a large gradient in the observations, which, for $L > 3.5$, is possible only at low energies (~100 keV). In turn, conditions (2) and 4 are associated with the strength of transport (whether convective or diffusive) and restrict the domain where the gradient is observed in the data; for example, condition 2 excludes low energy for $L > 3.5$. Condition 3 excludes the inner belt, and condition 4 excludes relativistic ($E\sim$ > 1 MeV) electrons below $L \sim 2.7$. Both of these regions are theoretically the ones where bottleneck-shaped distributions occur in the simulations (and hence where a steep gradient could be visible in the data). Condition 6 on the spacecraft latitude eliminates the range of large energy (~>500 keV) in the slot region ($L \sim 3$–3.5 and below) for latitude ~20°. These six conditions exclude a great part of the (L, E) plane. What remains is the region of $L \sim [3, 3.5]$ and $E \sim [100, 300]$ keV (with E increasing as L-shell diminishes) for which the bottleneck shape of the simulation corresponds to a steep gradient of the PSD. This is visible in Figure 6 (second column, first row, black lines). At 100 keV, both simulations (plain black line) and observations (dashed black line) show a 2-orders-of-magnitude difference between small and large pitch angles. The region where bottleneck distributions form (here $L \sim [3, 3.5]$ and $E \sim [100, 300]$ keV) is typically the region where the 1D model will fail at forming such a shape because the invariance of the lifetime with pitch angle does not allow the distribution shape to change nonuniformly in pitch angle. Lifetime only allows the decay of a preexisting pitch angle distribution shape. Here we show how restricted in (L, E) this region is, explaining partly the general good accuracy of the 1D-RFP model in the outer belt.

Another striking result concerns the so-called pocket of core electrons (700 keV to 2 MeV) in the outer belt. We find that the observed decay rates of this population are in very good agreement with simulations made with pitch angle diffusion only; Figure 6 shows the 1- and 2-MeV distributions simulated using pitch angle diffusion only (third line of Figure 6) match better the observations after 11 days of decay (second line of Figure 6 at $L = 4.5$) than the 3D simulations carried out with the combined radial, pitch angle, and energy diffusions. That would simply suggest an overestimation of the outer boundary condition high energy flux that injects too many core electrons, assuming correctness of both the transport mode and its rate for $L >$ ~4.
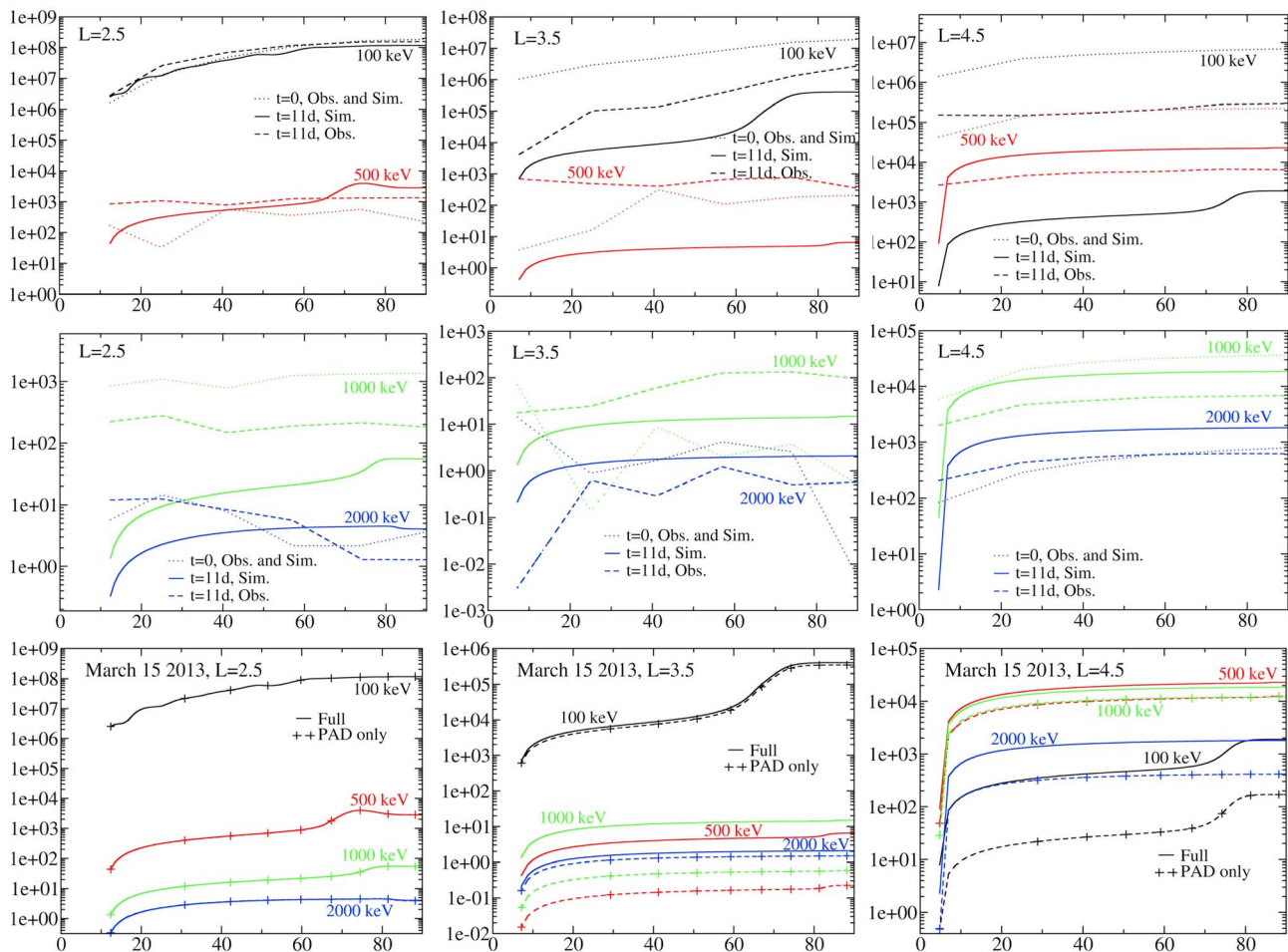
Figure 6. Pitch angle distribution (PAD in (c/MeV/cm)^3) at (left) $L = 2.5$, (middle) $L = 3.5$, (right) $L = 4.5$ for (first row) 100 and 500 keV and (second row) 1 and 2 MeV. (dotted line) Observations equate simulations on 4 March ($t = 0$). (plain line) Versatile Electron Radiation Belt (VERB-3D) simulations and (dashed line) observations are represented for the last day of the event on 15 March (noted $t = 11$ days). (third row) Results of (plain line) full VERB-3D simulations on 15 March (shown in the first and second rows) are compared with (dashed line with cross) pitch angle diffusion only simulations for (blue) 100, (red) 500, (green) 1,000, (blue) 2,000 keV.

The similarity between the pitch angle diffusion coefficients (for a wide (L, E, α_0) range) and the (inverse) lifetime is a new additional reason that explain why Lyons and Thorne (1973) found "the agreement is good, in fact embarrassingly so" between their "simplistic" 1D Fokker-Planck model and observations in the outer belt flux (for $L > 4$) since, as shown here, a lifetime becomes in that case an excellent approximation of the decay rates. But this result is independent of whether or not the radiation belt structure is at equilibrium (between radial transport and loss). Here daily variation in the flux snapshots of Figure 2 (and Figures 3 and 4) shows equilibrium is not reached, that is, $\partial f/\partial t \neq 0$. Besides, daily variations of the diffusion coefficients and boundary conditions do not allow equilibrium to exist, or, in other words, each set of $D\alpha_0\alpha_0$ and boundary condition leads to a different equilibrium solution (Loridan et al., 2017; Ripoll, Reeves et al., 2016). Running the simulations to longer times (in freezing the parameters) to establish when equilibrium is reached showed that great variations exist in the outer belt until at least 25 days and that equilibrium is reached after ~55 days in the outer belt ($L > 4$, $E < 4$ MeV).

7. Model Accuracy With Dedicated Metrics

The last section of this work is devoted to the quantification of the differences between observation and simulation thanks to two metrics, (i) the median symmetric accuracy (ζ) and (ii) the median log accuracy ratio (β), that are especially robust and well adapted to radiation belt electron flux since they conserve symmetry;
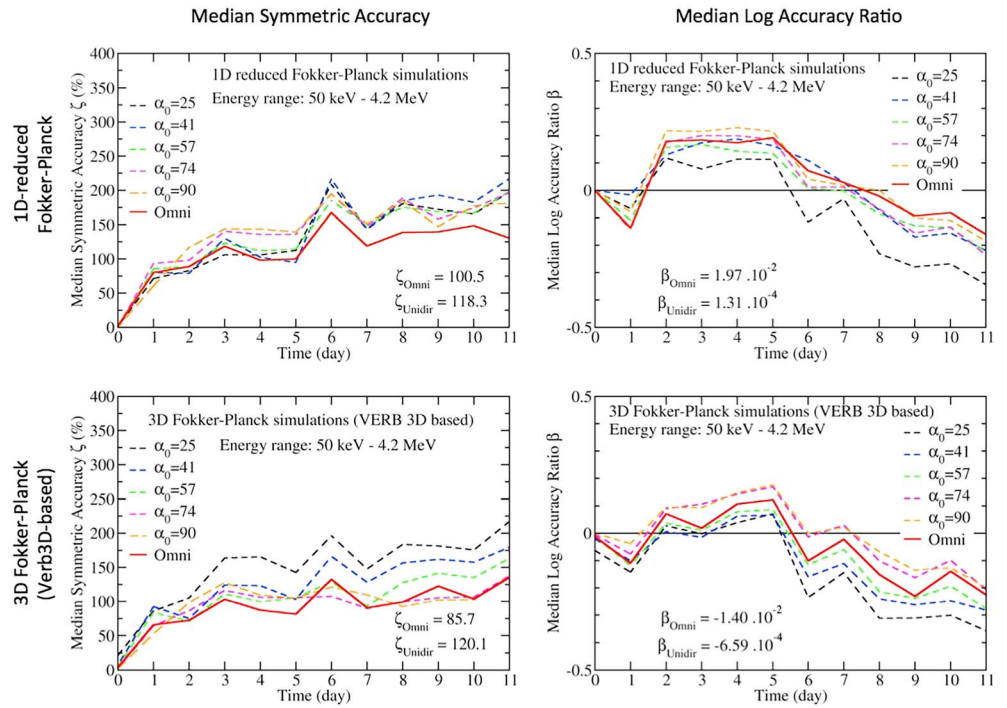
Figure 7. Daily evolution of the (left) median ($\log_{10}$) symmetric accuracy in percent (ζ) and (right) median ($\log_{10}$) accuracy ratio (β) from 4 March ($t = 0$) to 15 March ($t = 11$) 2013 of flux computed from (top) the 1D reduced Fokker-Planck model and (bottom) Versatile Electron Radiation Belt (VERB-3D; 3D Fokker-Planck based model) of either (dashed colored lines) directional flux at $\alpha_0 = 25°, 41°, 74°, 90°$ or (plain red line) the omnidirectional flux. Computations are made on the 50-keV to 4.2-MeV range of the Magnetic Electron and Ion Spectrometer (MagEIS) observations. Global values of ζ and β (in L, E, t) computed from the omnidirectional flux (ζ_{omni}) or over all unidirectional directions (ζ_{Unidir}) are written inside each figure providing a global accuracy rating of the simulations.

that is, overestimation and underestimation errors are equally graded (Morley, 2016; Brito & Morley, 2017). The median symmetric accuracy is

$$\zeta = 100 \times \left(10^{\text{Med}\left| \log_{10} Q_{\text{dir/omni}} \right|} - 1 \right)$$

and the median log accuracy ratio is

$$\beta = \text{Med}\left(\log_{10} Q_{\text{dir/omni}} \right)$$

with the accuracy ratio, Q (quotient), defined as $Q_{\text{dir}} = J^{\text{simu}}(E, \alpha_0, L, t)/J^{\text{RBSP}}(E, \alpha_0, L, t)$. The median function, Med, is taken over variables (E, α_0, L) in order to plot the indices evolution and over (E, α_0, L, t) to provide global (directional) indices over the 11-day period. For omnidirectional flux accuracy, we have $Q_{\text{omni}} = J^{\text{simu}}_{\text{omni}}(E, L, t)/J^{\text{RBSP}}_{\text{omni}}(E, L, t)$ and the median function is taken at time t over variables (E, L) and over (E, L, t) to provide single global (omnidirectional) indices. The largest values (in absolute value) of both the median symmetric accuracy and the median log accuracy ratio correspond to the largest error made by the model.

Figure 7 shows both metrics daily evolution from 4 March ($t = 0$) to 15 March ($t = 11$). Figure 7 also contains global time-integrated values that are discussed. The median symmetric accuracy percent is lower for the 3D results, with a global value of $\zeta_{\text{omni}} = 85\%$ over 11 days with the 3D model versus $\zeta_{\text{omni}} = 100\%$ with the 1D model. The error grows daily in Figure 7 from ~50% to ~150% over 11 days in 1D and from ~50% to ~120% over 11 days in 3D. Both models are close to the 100% error level representing a factor ~2 of accuracy of the simulated fluxes. Considering all possible inaccuracies from the measurements, theoretical approximations, and the absence of key measurements (e.g., the MLT dependence), an overall error bar of the omnidirectional fluxes of a factor ~2 is a good performance.
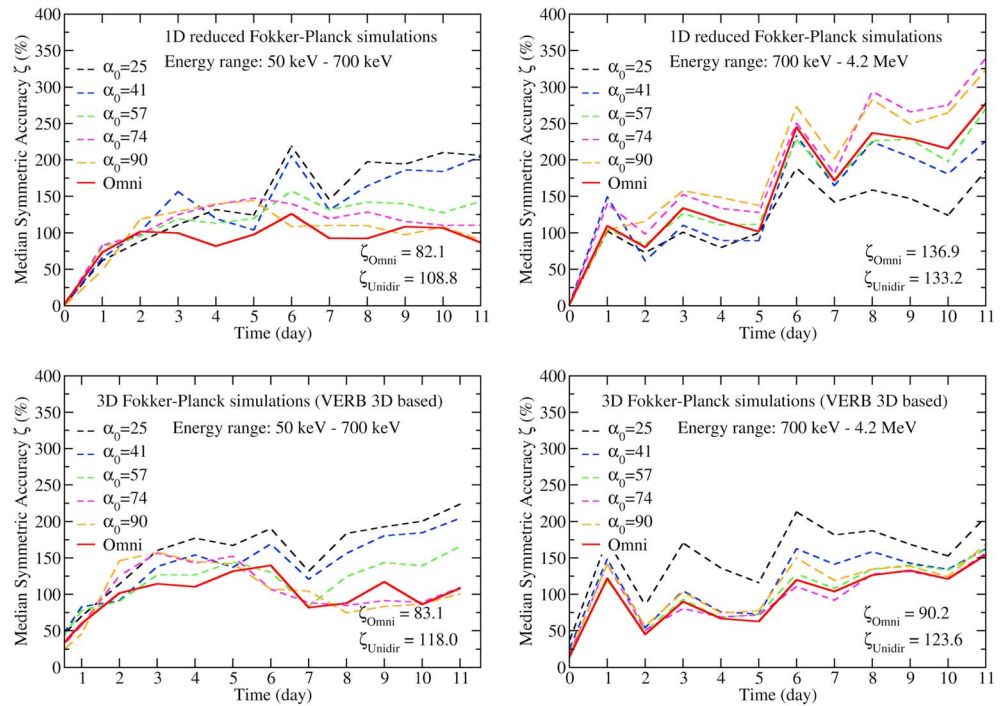
Figure 8. Daily evolution of the median ($\log_{10}$) symmetric accuracy in percent (ζ) from 4 March ($t = 0$) to 15 March ($t = 11$) 2013 of flux computed from (top) the 1D reduced Fokker-Planck model and (bottom) Versatile Electron Radiation Belt (VERB-3D; 3D Fokker-Planck based model) of either (dashed colored lines) directional flux at $\alpha_0 = 25°$, $41°$, $74°$, $90°$ or (plain red line) the omnidirectional flux. Computations are made on (left) the low-energy bin from 50 keV to 0.7 MeV and on (right) the high-energy bin from 0.7 to 4.2 MeV. Global values of ζ computed from the omnidirectional flux (ζ_{omni}) or over all unidirectional fluxes (ζ_{Unidir}) are written inside each figure providing a global accuracy rating of the simulations.

Figure 7 provides both omnidirectional metrics and unidirectional metrics in order to understand how the error is distributed in pitch angle and understand if it could affect our physical conclusions of sections 5 and 6 relative to the simulated 3D (L, E, α_0) belts structure. As expected, higher pitch angles are computed more accurately than lower ones in 3D. A larger error with the 1D model than with the 3D model at high pitch angle is consistent with the difference between lifetime and diffusion coefficients that increases as pitch angle increases, that is, above 60° as discussed in sections 5 and 6. In 1D, the error is more homogeneous in pitch angle due to the invariance of τ although more variations will be found below when the energy is binned. The omnidirectional median symmetric accuracy turns out to be lower than all unidirectional median symmetric accuracy in 1D in Figure 7 (top, left), which is counterintuitive. But the omnidirectional median symmetric accuracy is computed directly from $J_{omni}^{simu}(E, L, t)$ and $J_{omni}^{RBSP}(E, L, t)$ and is not a pitch angle average of the unidirectional median symmetric accuracy (cf. mathematic definitions above). However, we have checked that averaging the unidirectional median symmetric accuracy with respect to pitch angle (not plotted) does give a pitch angle-averaged median symmetric accuracy (which one could assimilate to a omni-directional metric) that is indeed above the omnidirectional median symmetric accuracy and consistently located between both the minimum and maximum unidirectional median symmetric accuracy.

The median log accuracy ratio (β) is a robust measure of bias that is positive if the model overestimates the data and vice versa. Three-dimensional results are again more accurate than 1D results with, for instance, a factor 2 difference in β for the first 5 days. The time-varying β shows the 1D model overestimates the flux ($2 < t < 6$ days) in comparison to the 3D model. Conversely, the 3D model underestimates the flux ($6 < t < 11$ days) in comparison to the 1D model.

Splitting the energy in two bands, one low-energy band (leb) $E < 700$ keV in Figure 8 (left) and one high-energy band (heb) $E > 700$ keV in Figure 8 (right), we find $\zeta_{leb} = 82\%$ and $\zeta_{heb} = 137\%$ with the 1D model and $\zeta_{leb} = 83\%$ and $\zeta_{heb} = 90\%$ with the 3D model. This shows the 3D model performs equally well on

global average in energy and better than the 1D model whose accuracy is lower for the high-energy band. Looking at daily variations of the unidirectional median symmetric accuracy, the latter diminishes as pitch angle increases for both the low-energy band and the high-energy band in Figure 8, similarly to all energy bands in Figure 7. However, unidirectional median symmetric accuracy of the 1D model diminishes as pitch angle decreases for the low-energy band and, reversely, increases as pitch angle decreases for the high-energy band. Variations in unidirectional median symmetric accuracy are higher for the high-energy bin, with a factor ~2 between the median symmetric accuracy of 25° electrons (150%) and the median symmetric accuracy of 90° electrons (325%). The highest median symmetric accuracy, that is, the largest error after 11 days, is then ~×4 (325%) for $\alpha > 75°$ and $E > 700$ keV (1D model), which is almost twice higher than the unidirectional median symmetric accuracy of the 3D model, that is, 150% for $\alpha > 75°$ and $E > 700$ keV. These metrics behaviors are consistent and illustrative of the overestimation of the so-called pocket of core electrons (700 keV to 2 MeV) in the outer belt (cf. sections 5 and 6) and the fact that error is maximal in 1D for high energy and high pitch angle. Variation in energy of the median log accuracy ratio, β, is similar to ζ (not shown). However, the 1D model leads to an overestimated flux in the high-energy band, while the 3D one slightly underestimates the data.

These metrics provide additional evidence that losses are overestimated because of the inaccuracy of the low-energy injections that are not modeled. However, our main concern remains the overestimation of the outer belt, particularly above 700 keV, regardless of the model.

8. Conclusions

We studied the evolution of the L-shell, energy, and pitch angle structure of the radiation belts during the storm recovery phase 4–15 March 2013 using MagEIS observations and both 1D-RFP and 3D Fokker-Planck simulations using VERB-3D. These models use consistent event-driven pitch angle diffusion coefficients or lifetimes from whistler mode hiss waves. Both models reproduce fairly well the daily flux dynamics observed with MagEIS. The accuracy of the two models is further measured in detail with dedicated local and global metrics. The global median symmetric accuracy of the omnidirectional flux is ~100% (factor of ~2) with the 1D model and, better, 85% with the 3D model. This qualifies both models in their ability to describe accurately the global (t, L, E, α_0) structure of the belts for short quiet periods that follow storms (as soon as the plasmasphere is well extended enough to prohibit the existence of chorus waves and local acceleration). Local discrepancies can be larger, with the largest median symmetric accuracy of the directional flux built up after 11 days of ~325% for outer belt's electrons with both high pitch angle (>75°) and large energy (>700 keV) for the 1D model, being about twice lower (~150%) with the 3D model.

The (L, E, α_0) structure of decaying trapped electrons is made of a pitch angle-dependent inner belt of electrons below 900 keV preserved from hiss wave scattering in its core and with its dynamic outer edge eroded by hiss waves. The slot is formed in 11 days. Slot and outer belt decays are quite homogeneous in pitch angle for $\alpha_0 \sim <60°$ above $L \sim 3.5$ due to the homogeneity of the pitch angle diffusion coefficients, itself inherited of the wave properties. Since $D\alpha_0\alpha_0(\alpha_0) \sim 1/\tau$ for $\alpha_0 \sim <60°$ and $L > ~3.5$, both lifetimes in 1D and diffusion coefficients in 3D lead to accurate simulations of the slot and outer belt dynamic quasi pitch angle-independent decay. In contrast, bottleneck-shaped distributions indicative of distinct dynamics for low/high pitch angles are found in the slot region for $L \sim$ [3, 3.5] and $E \sim$ [100, 300] keV (with E increasing as L-shell diminishes). Conditions to fulfill for observing a bottleneck-shaped distribution are given in section 6.

The outer belt ends up with an S-shape on its inner edge. The trapped outer belt electrons are located within a two-region structure in (L, E) with a fading region in between ($L \sim$ [4.5, 5.5] and $E \sim$ [200, 500] keV) appearing in the process of the slot formation. Simulation predicts that intense and/or long-duration hiss scattering (without injections) produces an outer belt made of only these two isolated regions (as soon as not replenished by new incoming electrons). Below 100 keV is a low-energy seed population centered at $L \sim 5$, with local hourly/daily injections often filling all the L-shells down to the inner belt. The second region is a core radiation belt population of high-energy trapped electrons ($L \sim$ [4.5, 5.5] and $E \sim$ [0.7, 2] MeV) with edges fading with the hiss duration and intensity. This region is also preserved from electromagnetic ion cyclotron wave scattering due to the rather low energy (<2 MeV) (e.g., Kersten et al., 2014; Usanova et al., 2014). This structure persists due to the wide extension of the plasmasphere allowing the existence of intense hiss and wave-particle interactions in the absence of chorus waves and local acceleration.

References

Abel, B., & Thorne, R. M. (1998). Electron scattering and loss in Earth's inner magnetosphere, 1: Dominant physical processes. *Journal of Geophysical Research*, *103*(A2), 2385–2396. https://doi.org/10.1029/97JA02919

Albert, J. M. (1994). Quasi-linear pitch-angle diffusion coefficients: Retaining high harmonics. *Journal of Geophysical Research*, *99*(A12), 23,741–23,745. https://doi.org/10.1029/94JA02345

Albert, J. M. (1999). Analysis of quasi-linear diffusion coefficients. *Journal of Geophysical Research*, *104*, 2419.

Albert, J. M. (2005). Evaluation of quasi-linear diffusion coefficients for whistler mode waves in a plasma with arbitrary density ratio. *Journal of Geophysical Research*, *110*, A03218. https://doi.org/10.1029/2004JA010844

Albert, J. M. (2012). Dependence of quasi-linear diffusion coefficients on wave parameters. *Journal of Geophysical Research*, *117*, A09224. https://doi.org/10.1029/2012JA017718

Aseev, N. A., Shprits, Y. Y., Drozdov, A. Y., & Kellerman, A. C. (2016). Numerical applications of the advective-diffusive codes for the inner magnetosphere. *Space Weather*, *14*, 993–1010. https://doi.org/10.1002/2016SW001484

Baker, D. N., Baker, D. N., Jaynes, A. N., Li, X., Henderson, M. G., Kanekal, S. G., et al. (2014). Gradual diffusion and punctuated phase space density enhancements of highly relativistic electrons: Van Allen Probes observations. *Geophysical Research Letters*, *41*, 1351–1358. https://doi.org/10.1002/2013GL058942

Blake, J. B., Carranza, P. A., Claudepierre, S. G., Clemmons, J. H., Crain, W. R., Dotan, Y., et al. (2013). The Magnetic Electron Ion Spectrometer (MagEIS) instruments aboard the Radiation Belt Storm Probes (RBSP) spacecraft. *Space Science Reviews*, *179*(1-4), 383–421. https://doi.org/10.1007/s11214-013-9991-8

Boyd, A. J., Spence, H. E., Claudepierre, S. G., Fennell, J. F., Blake, J. B., Baker, D. N., Reeves, G. D., et al. (2014). Quantifying the radiation belt seed population in the March 17, 2013 electron acceleration event. *Geophysical Research Letters*, *41*, 2275–2281. https://doi.org/10.1002/2014GL059626

Brito, T., Hudson, M. K., Kress, B., Paral, J., Halford, A., Millan, R., & Usanova, M. (2015). Simulation of ULF wave-modulated radiation belt electron precipitation during the 17 March 2013 storm. *Journal of Geophysical Research: Space Physics*, *120*, 3444–3461. https://doi.org/10.1002/2014JA020838

Brito, T. V., & Morley, S. K. (2017). Improving empirical magnetic field models by fitting to in situ data using an optimized parameter approach. *Space Weather*, *15*, 1628–1648. https://doi.org/10.1002/2017SW001702

Claudepierre, S. G., O'Brien, T. P., Blake, J. B., Fennell, J. F., Roeder, J. L., Clemmons, J. H., et al. (2015). A background correction algorithm for Van Allen Probes MagEIS electron flux measurements. *Journal of Geophysical Research: Space Physics*, *120*, 5703–5727. https://doi.org/10.1002/2014JA020876

Drozdov, A. Y., Shprits, Y. Y., Orlova, K. G., Kellerman, A. C., Subbotin, D. A., Baker, D. N., et al. (2015). Energetic, relativistic, and ultrarelativistic electrons: Comparison of long-term VERB code simulations with Van Allen Probes measurements. *Journal of Geophysical Research: Space Physics*, *120*, 3574–3587. https://doi.org/10.1002/ 2014JA020637

Fennell, J. F., Claudepierre, S. G., Blake, J. B., O'Brien, T. P., Clemmons, J. H., Baker, D. N., et al. (2015). Van Allen Probes show that the inner radiation zone contains no MeV electrons: ECT/MagEIS data. *Geophysical Research Letters*, *42*, 1283–1289. https://doi.org/10.1002/2014GL062874

Gao, Y., Xiao, F., Yan, Q., Yang, C., Liu, S., He, Y., & Zhou, Q. (2015). Influence of wave normal angles on hiss-electron interaction in Earth's slot region. *Journal of Geophysical Research: Space Physics*, *120*, 9385–9400. https://doi.org/10.1002/2015JA021786

Hudson, M. K., Paral, J., Kress, B. T., Wiltberger, M., Baker, D. N., Foster, J. C., et al. (2015). Modeling CME-shock-driven storms in 2012–2013: MHD test particle simulations. *Journal of Geophysical Research: Space Physics*, *120*, 1168–1181. https://doi.org/10.1002/ 2014JA020833

Jaynes, A. N., Baker, D. N., Singer, H. J., Rodriguez, J. V., Loto'aniu, T. M., Ali, A. F., et al. (2015). Source and seed populations for relativistic electrons: Their roles in radiation belt changes. *Journal of Geophysical Research: Space Physics*, *120*, 7240–7254. https://doi.org/10.1002/ 2015JA021234

Kersten, T., Horne, R. B., Glauert, S. A., Meredith, N. P., Fraser, B. J., & Grew, R. S. (2014). Electron losses from the radiation belts caused by EMIC waves. *Journal of Geophysical Research: Space Physics*, *119*, 8820–8837. https://doi.org/10.1002/2014JA020366

Kim, K.-C., Shprits, Y., Subbotin, D., & Ni, B. (2011). Understanding the dynamic evolution of the relativistic electron slot region including radial and pitch-angle diffusion. *Journal of Geophysical Research*, *116*, A10214. https://doi.org/10.1029/2011JA016684

Kletzing, C. A., Kurth, W. S., Acuna, M., MacDowall, R. J., Torbert, R. B., Averkamp, T., et al. (2013). The electric and magnetic field instrument suite and integrated science (EMFISIS) on RBSP. *Space Science Reviews*, *179*(1-4), 127–181. https://doi.org/10.1007/s11214-013-9993-6

Kurth, W. S., De Pascuale, S., Faden, J. B., Kletzing, C. A., Hospodarsky, G. B., Thaller, S., & Wygant, J. R. (2015). Electron densities inferred from plasma wave spectra obtained by the waves instrument on Van Allen Probes. *Journal of Geophysical Research: Space Physics*, *120*, 904–914. https://doi.org/10.1002/2014JA020857

Lejosne, S., Kunduri, B. S. R., Mozer, F. S., & Turner, D. L. (2018). Energetic electron injections deep into the inner magnetosphere: A result of the subauroral polarization stream (SAPS) potential drop. *Geophysical Research Letters*, *45*, 3811–3819. https://doi.org/10.1029/2018GL077969

Li, W., Ni, B., Thorne, R. M., Bortnik, J., Nishimura, Y., Green, J. C., et al. (2014). Quantifying hiss-driven energetic electron precipitation: A detailed conjunction event analysis. *Geophysical Research Letters*, *41*, 1085–1092. https://doi.org/10.1002/2013GL059132

Li, Z., Hudson, M., Jaynes, A., Boyd, A., Malaspina, D., Thaller, S., et al. (2014). Modeling gradual diffusion changes in radiation belt electron phase space density for the March 2013 Van Allen Probes case study. *Journal of Geophysical Research: Space Physics*, *119*, 8396–8403. https://doi.org/10.1002/2014JA020359

Loridan, V., Ripoll, J.-F., & de Vuyst, F. (2017). The analytical solution of the transient radial diffusion equation with a nonuniform loss term. *Journal of Geophysical Research: Space Physics*, *122*, 5979–6006. https://doi.org/10.1002/2017JA023868

Lyons, L. R., & Thorne, R. M. (1973). Equilibrium structure of radiation belt electrons. *Journal of Geophysical Research*, *78*(13), 2142–2149. https://doi.org/10.1029/ JA078i013p02142

Lyons, L. R., Thorne, R. M., & Kennel, C. F. (1972). Pitch-angle diffusion of radiation belt electrons within the plasmasphere. *Journal of Geophysical Research*, *77*(19), 3455–3474. https://doi.org/10.1029/JA077i019p03455

Ma, Q., Li, W., Thorne, R. M., Bortnik, J., Reeves, G. D., Kletzing, C. A., et al. (2016). Characteristic energy range of electron scattering due to plasmaspheric hiss. *Journal of Geophysical Research: Space Physics*, *121*, 11,737–11,749. https://doi.org/10.1002/2016JA023311

Ma, Q., Mourenas, D., Li, W., Artemyev, A., & Thorne, R. M. (2017). VLF waves from ground based transmitters observed by the Van Allen Probes: Statistical model and effects on plasmaspheric electrons. *Geophysical Research Letters*, *44*, 6483–6491. https://doi.org/10.1002/ 2017GL073885

Malaspina, D. M., Jaynes, A. N., Hospodarsky, G., Bortnik, J., Ergun, R. E., & Wygant, J. (2017). Statistical properties of low-frequency plasma-spheric hiss. *Journal of Geophysical Research: Space Physics*, *122*, 8340–8352. https://doi.org/10.1002/2017JA024328

Malaspina, D. M., Ripoll, J.-F., Chu, X., Hospodarsky, G., & Wygant, J. (2018). Variation in plasmaspheric hiss wave power with plasma density. *Geophysical Research Letters*, *45*(18), 9417–9426. https://doi.org/10.1029/2018GL078564

Meredith, N. P., Horne, R. B., Glauert, S. A., Baker, D. N., Kanekal, S. G., & Albert, J. M. (2009). Relativistic electron loss timescales in the slot region. *Journal of Geophysical Research*, *114*, A03222. https://doi.org/10.1029/2008JA013889

Meredith, N. P., Horne, R. B., Li, W., Thorne, R. M., & Sicard-Piet, A. (2014). Global model of low-frequency chorus ($f_{LHR} < f < 0.1 f_{ce}$) from multiple satellite observations. *Geophysical Research Letters*, *41*, 280–286. https://doi.org/10.1002/2013GL059050

Morley, S. K. (2016). *Alternatives to accuracy and bias metrics based on percentage errors for radiation belt modeling applications* (Tech. Rep. LA-UR-16-24592). Los Alamos, NM: Los Alamos National Laboratory. https://doi.org/10.2172/1260362

Ni, B., Bortnik, J., Thorne, R. M., Ma, Q., & Chen, L. (2013). Resonant scattering and resultant pitch angle evolution of relativistic electrons by plasmaspheric hiss. *Journal of Geophysical Research: Space Physics*, *118*, 7740–7751. https://doi.org/10.1002/2013JA019260

Ni, B., Li, W., Thorne, R. M., Bortnik, J., Ma, Q., Chen, L., et al. (2014). Resonant scattering of energetic electrons by unusual low-frequency hiss. *Geophysical Research Letters*, *41*, 1854–1861. https://doi.org/10.1002/2014GL059389

Ozeke, L. G., Mann, I. R., Murphy, K. R., Jonathan Rae, I., & Milling, D. K. (2014). Analytic expressions for ULF wave radiation belt radial diffusion coefficients. *Journal of Geophysical Research: Space Physics*, *119*, 1587–1605. https://doi.org/10.1002/2013JA019204

Reeves, G. D., Friedel, R. M. W., Larsen, B. A., Skoug, R. M., Funsten, H. O., Claudeoierre, S. G., et al. (2015). Energy-dependent dynamics of keV to MeV electrons in the inner zone, outer zone, and slot regions. *Journal of Geophysical Research: Space Physics*, *121*, 397–412. https://doi.org/10.1002/2015JA021569

Réveillé, T., Bertrand, P., Ghizzo, A., Simonet, F., & Baussart, N. (2001). Dynamic evolution of relativistic electrons in the radiation belts. *Journal of Geophysical Research*, *106*(A9), 18,883–18,894. https://doi.org/10.1029/2000JA900177

Ripoll, J.-F., Albert, J. M., & Cunningham, G. S. (2014). Electron lifetimes from narrowband wave-particle interactions within the plasmasphere. *Journal of Geophysical Research: Space Physics*, *119*, 8858–8880. https://doi.org/10.1002/2014JA020217

Ripoll, J.-F., Chen, Y., Fennell, J. F., & Friedel, R. H. W. (2014). On long decays of electrons in the vicinity of the slot region observed by HEO3. *Journal of Geophysical Research: Space Physics*, *120*, 460–478. https://doi.org/10.1002/2014JA020449

Ripoll, J.-F., Loridan, V., Cunningham, G. S., Reeves, G. D., & Shprits, Y. Y. (2016). On the time needed to reach an equilibrium structure of the radiation belts. *Journal of Geophysical Research: Space Physics*, *121*, 7684–7698. https://doi.org/10.1002/2015JA022207

Ripoll, J.-F., & Mourenas, D. (2012). High-energy electron diffusion by resonant interactions with whistler mode hiss. In D. Summers et al. (Eds.), *Dynamics of the Earth's Radiation Belts and Inner Magnetosphere, Geophysical Monograph Series* (Vol. 199, pp. 281–289). American Geophyscial Union.

Ripoll, J.-F., Reeves, G. D., Cunningham, G. S., Loridan, V., Denton, M., Santolík, O., et al. (2016). Reproducing the observed energy-dependent structure of Earth's electron radiation belts during storm recovery with an event-specific diffusion model. *Geophysical Research Letters*, *43*, 5616–5625. https://doi.org/10.1002/2016GL068869

Ripoll, J.-F., Santolík, O., Reeves, G. D., Kurth, W. S., Denton, M. H., Loridan, V., et al. (2017). Effects of whistler mode hiss waves in march 2013. *Journal of Geophysical Research: Space Physics*, *122*, 7433–7462. https://doi.org/10.1002/2017JA024139

Santolík, O., Parrot, M., & Lefeuvre, F. (2003). Singular value decomposition methods for wave propagation analysis. *Radio Science*, *38*(1), 1010. https://doi.org/10.1029/2000RS002523

Santolik, O., Parrot, M., Storey, L. R. O., Pickett, J., & Gurnett, D. A. (2001). Propagation analysis of plasmaspheric hiss using polar PWI mea-surements. *Geophysical Research Letters*, *28*(6), 1127–1130. https://doi.org/10.1029/2000GL012239

Schulz, M., & Lanzerotti, L. (1974). *Particle diffusion in the radiation belts*. New York: Springer. https://doi.org/10.1007/978-3-642-65675-0

Selesnick, R. S., Albert, J. M., & Starks, M. J. (2013). Influence of a ground-based VLF radio transmitter on the inner electron radiation belt. *Journal of Geophysical Research: Space Physics*, *118*, 628–635. https://doi.org/10.1002/jgra.50095

Shprits, Y. Y., Kellerman, A. C., Drozdov, A. Y., Spence, H. E., Reeves, G. D., & Baker, D. N. (2015). Combined convective and diffusive simulations: VERB-4D comparison with 17 March 2013 Van Allen Probes observations. *Geophysical Research Letters*, *42*, 9600–9608. https://doi.org/10.1002/2015GL065230

Shprits, Y. Y., Subbotin, D., & Ni, B. (2009). Evolution of electron fluxes in the outer radiation belt computed with the VERB code. *Journal of Geophysical Research*, *114*, A11209. https://doi.org/10.1029/2008JA013784

Shprits, Y. Y., Subbotin, D. A., Meredith, N. P., & Elkington, S. R. (2008). Review of modeling of losses and sources of relativistic electrons in the outer radiation belts: II. Local acceleration and loss. *Journal of Atmospheric and Solar-Terrestrial Physics*, *70*(14), 1694–1713. https://doi.org/10.1016/j.jastp.2008.06.014

Spasojevic, M., Shprits, Y. Y., & Orlova, K. (2015). Global empirical models of plasmaspheric hiss using Van Allen Probes. *Journal of Geophysical Research: Space Physics*, *120*, 10,370–10,383. https://doi.org/10.1002/2015JA021803

Subbotin, D. A., & Shprits, Y. Y. (2009). Three-dimensional modeling of the radiation belts using the Versatile Electron Radiation Belt (VERB) code. *Space Weather*, *7*, S10001. https://doi.org/10.1029/2008SW000452

Subbotin, D. A., Shprits, Y. Y., & Ni, B. (2010). Three-dimensional VERB radiation belt simulations including mixed diffusion. *Journal of Geophysical Research*, *115*, A03205. https://doi.org/10.1029/2009JA015070

Subbotin, D. A., Shprits, Y. Y., & Ni, B. (2011). Long-term radiation belt simulation with the VERB 3-D code: Comparison with CRRES obser-vations. *Journal of Geophysical Research*, *116*, A12210. https://doi.org/10.1029/2011JA017019

Thaller, S. A., Wygant, J. R., Dai, L., Breneman, A. W., Kersten, K., Cattell, C. A., et al. (2015). Van Allen Probes investigation of the large-scale duskward electric field and its role in ring current formation and plasmasphere erosion in the 1 June 2013 storm. *Journal of Geophysical Research: Space Physics*, *120*, 4531–4543. https://doi.org/10.1002/2014JA020875

Tsyganenko, N. A. (1989). A magnetospheric magnetic field model with a warped tail current sheet. *Planetary and Space Science*, *37*(1), 5–20. https://doi.org/10.1016/0032-0633(89)90066-4

Turner, D. L., Claudepierre, S. G., Fennell, J. F., O'Brien, T. P., Blake, J. B., Lemon, C., et al. (2015). Energetic electron injections deep into the inner magnetosphere associated with substorm activity. *Geophysical Research Letters*, *42*, 2079–2087. https://doi.org/10.1002/2015gl063225

Turner, D. L., O'Brien, T. P., Fennell, J. F., Claudepierre, S. G., Blake, J. B., Jaynes, A. N., et al. (2016). Investigating the source of near-relativistic and relativistic electrons in Earth's inner radiation belt. *Journal of Geophysical Research: Space Physics*, *122*, 695–710. https://doi.org/10.1002/2016JA023600

Ukhorskiy, A. Y., & Sitnov, M. (2008). Radial transport in the outer radiation belt due to global magnetospheric compressions. *Journal of Atmospheric and Solar-Terrestrial Physics*, *70*, 1714–1726.

Ukhorskiy, A. Y., & Sitnov, M. I. (2012). Dynamics of radiation belt particles. *Space Science Reviews*, *179*, 545–578. https://doi.org/10.1007/s11214-012-9938-5

Usanova, M. E., Drozdov, A., Orlova, K., Mann, I. R., Shprits, Y., Robertson, M. T., et al. (2014). Effect of EMIC waves on relativistic and ultrarelativistic electron populations: Ground-based and Van Allen probes observations. *Geophysical Research Letters*, *41*, 1375–1381. https://doi.org/10.1002/2013GL059024

Walt, M. (1970). Radial diffusion of trapped particles. In B. M. McCormac (Ed.), *Particles and fields in the magnetosphere* (pp. 410–415). Dordrecht, Holland: D. Reidel.

Watt, C. E. J., Rae, I. J., Murphy, K. R., Anekallu, C., Bentley, S. N., & Forsyth, C. (2017). The parameterization of wave-particle interactions in the outer radiation belt. *Journal of Geophysical Research: Space Physics*, *122*, 9545–9551. https://doi.org/10.1002/2017JA024339

Xiao, F., Yang, C., He, Z., Su, Z., Zhou, Q., He, Y., et al. (2014). Chorus acceleration of radiation belt relativistic electrons during March 2013 geomagnetic storm. *Journal of Geophysical Research: Space Physics*, *119*, 3325–3332. https://doi.org/10.1002/2014JA019822

Yu, Y., Jordanova, V., Welling, D., Larsen, B., Claudepierre, S. G., & Kletzing, C. (2014). The role of ring current particle injections: Global simulations and Van Allen Probes observations during 17 March 2013 storm. *Geophysical Research Letters*, *41*, 1126–1132. https://doi.org/10.1002/2014GL059322

Zhao, H., Baker, D. N., Califf, S., Li, X., Jaynes, A. N., Leonard, T., et al. (2017). Van Allen Probes measurements of energetic particle deep penetration into the low L region ($L < 4$) during the storm on 8 April 2016. *Journal of Geophysical Research: Space Physics*, *122*, 12,140–12,152. https://doi.org/10.1002/2017JA024558